





## Comparative study of electrooptic, dielectric, and structural properties of two glassforming antiferroelectric mixtures with a high tilt angle

Aleksandra Deptuch <sup>1,\*</sup>, Sebastian Lalik,<sup>2</sup> Małgorzata Jasiurkowska-Delaporte,<sup>1</sup> Ewa Juszyńska-Gałązka <sup>1</sup>,  
Anna Drzewicz <sup>1</sup>, Magdalena Urbańska,<sup>3</sup> and Monika Marzec <sup>2</sup>

<sup>1</sup>*Institute of Nuclear Physics Polish Academy of Sciences, Radzikowskiego 152, PL-31342 Kraków, Poland*

<sup>2</sup>*M. Smoluchowski Institute of Physics, Jagiellonian University, Łojasiewicza 11, PL-30348 Kraków, Poland*

<sup>3</sup>*Institute of Chemistry, Military University of Technology, Kaliskiego 2, PL-00908 Warsaw, Poland*



(Received 13 September 2021; accepted 6 February 2022; published 22 February 2022)

Vitrification of the antiferroelectric smectic- $C_A^*$  phase is reported for the orthoconic mixture W-1000 and its new derivative W-356. The crystallization is not observed even upon slow cooling and the cold crystallization on subsequent heating is also absent. Molecular dynamics in the smectic phases of both mixtures is investigated down to 173 K and the fragility parameters are determined from the temperature behavior of the  $\alpha$ -process. X-ray diffraction is applied to compare the structural parameters of W-356 and W-1000 as well as to study the structural changes during the glass transition of the Sm- $C_A^*$  phase. The evolution of the smectic layer order within the Sm- $C_A^*$  glass is reported, while the correlation length of the short-range order in the smectic layers is shown to be almost constant below the glass transition temperature. Electrooptic properties of W-356: spontaneous polarization, tilt angle and switching time are determined and compared with these of W-1000. The observed differences between the properties of W-356 and W-1000 might be explained by the dimer formation of components with the  $-C \equiv N$  terminal group, present only in the W-356 mixture, and by the different structure of the aromatic molecular core in one of the W-356 components.

DOI: [10.1103/PhysRevE.105.024705](https://doi.org/10.1103/PhysRevE.105.024705)

### I. INTRODUCTION

The tilted smectic phases of chiral compounds with a nonzero molecular dipole moment can show ferro- or antiferroelectric properties after unwinding of their helical structure, which can be observed as a switching of molecules by an external electric field [1–3]. Orthoconic smectic phases (with the tilt angle close or equal to  $45^\circ$ ) allow us to obtain the full extinction of the transmitted light for a sample contained between crossed polarizers even with some defects in the sample's alignment, which is more difficult to obtain for other tilt angle values [4,5]. Because of this property, the orthoconic liquid crystals have the best chance of being used in liquid crystal displays (LCDs) [6]. Another class of mesomorphic compounds with potential applications are liquid crystalline glassformers. Such glasses show the long-range orientational order and various degree of the positional order depending on the vitrified mesophase, therefore they can be further used in optical and electronic devices [7–12]. Moreover, smectic glassformers enable investigation of influence of the glass transition on the quasi-long-range positional order, which cannot be done for classical glasses or nematic glassformers.

One of the most promising orthoconic liquid crystalline mixtures is the eutectic binary W-1000 mixture [13–15] and its modifications [16–24]. The components of W-1000 are 3F5HPhF6 and 3F7FPhH6 (Fig. 1 and Table I) from

the family of  $3FmX_1PhX_2r$  fluorinated esters [25–29]. The phase sequence of W-1000 is as follows: smectic- $C_A^*$  (374 K) smectic- $C^*$  (376.7 K) smectic- $A^*$  (379.1 K) isotropic liquid [13]. These smectic phases, presented schematically in Fig. 1, will be further abbreviated as Sm- $C_A^*$ , Sm- $C^*$ , and Sm- $A^*$ , respectively. The antiferroelectric Sm- $C_A^*$  phase of W-1000 was observed on cooling in a wide temperature range down to 250 K and the crystallization of W-1000 was not reported [15]. One of the components of W-1000, 3F5HPhF6, exhibits the vitrified Sm- $C_A^*$  phase [27], which implies that W-1000 is a glassformer as well, although, up to our knowledge, its vitrification has not been reported and studied in details yet.

Taking it into account, the main aim of this paper is investigation of the glass transition of the Sm- $C_A^*$  phase in the W-1000 mixture and its new modification W-356, doped with two compounds, denoted here as C1 and C2, possessing the  $-C \equiv N$  terminal group [30] (Fig. 1 and Table I). Molecular dynamics in the supercooled ( $\alpha$ -process) and vitrified (secondary  $\beta$ -process and  $\gamma$ -process) Sm- $C_A^*$  phase will be discussed and the fragility index of both mixtures will be determined. The structural changes within the Sm- $C_A^*$  phase during the glass transition, involving the smectic layer order and short-range order within the smectic layers, will be presented. Our another aim is the detailed investigation of the physical properties of the new W-356 mixture, which will be compared with the respective results for the base W-1000 mixture. The experimental methods include differential scanning calorimetry (DSC), polarizing optical microscopy (POM), electrooptic measurements, broadband dielectric spectroscopy (BDS), and x-ray diffraction (XRD).

\*Corresponding author: [aleksandra.deptuch@ifj.edu.pl](mailto:aleksandra.deptuch@ifj.edu.pl)

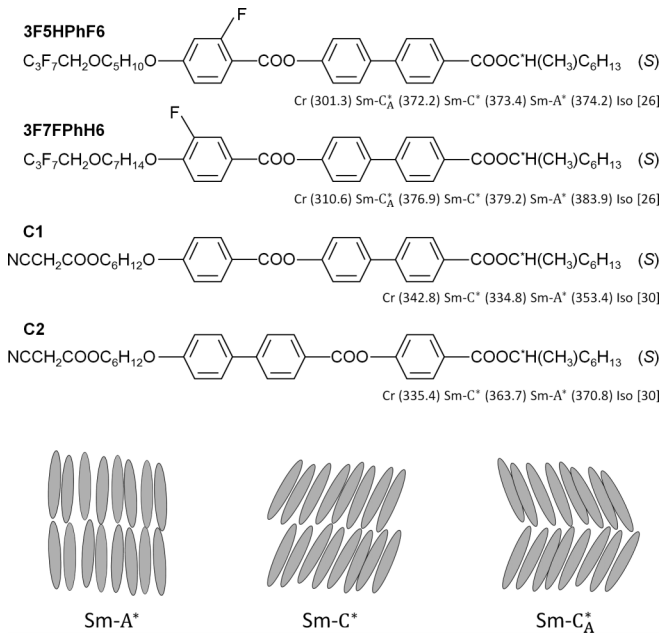


FIG. 1. Components of the W-1000 and W-356 mixtures and schemes of the molecular arrangement in the smectic-A\*, -C\*, and -C<sub>A</sub>\* phases.

PM7 and DFT calculations for isolated molecules of the components of both mixtures are also performed to estimate molecular size, dipole moments and energy barriers for selected intramolecular rotations.

## II. EXPERIMENTAL DETAILS

W-1000 and W-356 mixtures were prepared in the Institute of Chemistry of the Military University of Technology in Warsaw. The synthesis of the 3F5HPhF6 and 3F7FPhH6 compounds is described in Ref. [25] and synthesis of the C1 and C2 compounds is presented in Refs. [30,31].

Differential scanning calorimetry (DSC) measurements were done with DSC-2500 (TA Instruments, U.S.) calorimeter for the 24.820 mg sample of W-1000 and the 16.740 mg sample of W-356 contained within aluminum pans. Each sample was initially heated to 393 K, above the temperature of the transition to isotropic liquid, then cooled down to 153 K and heated back to 393 K with 2, 5, 10, 15, and 20 K/min rates. Data analysis was done in TRIOS software.

Polarizing optical microscopy (POM) texture observations were done using Leica DM2700 P (Leica Microsystems, Germany) polarizing microscope with Linkam (UK) temperature attachment for the samples between two microscopic slides without aligning layers. Transition temperatures between the smectic phases were determined during cooling with 2 K/min rate. The numerical analysis of textures was performed with the TOApy program [32].

Electrooptic measurements were performed by using ECLIPSE LV100POL polarizing microscope (Nikon, Japan) equipped with WTMS-14C temperature controller (Fine Instruments, Poland), 33120A generator (Agilent Technologies, U.S.), F20ADI amplifier (FLC Electronics, Sweden), DSO6102A oscilloscope (Agilent Technologies, U.S.), and

PD02 photodetector (INSTEC, U.S.). The samples were introduced by the capillary effect to the ITO electrooptic cells (4.9 μm thickness, planar alignment, AWAT company, Poland). Before measurements, each sample was heated up to isotropic liquid and cooled down to the Sm-C\* phase (to 369 K for W-1000 and 361 K for W-356), where the electric field was applied (square wave) to obtain the uniformly aligned samples (it took ca. 1 h and 1.5 h for W-1000 and W-356, respectively). Next, the samples were heated to the vicinity of the Sm-C\* → Sm-A\* transition and the electrooptic measurements were carried out on cooling ( $V_{pp} = 120$  V, 50 Hz). The spontaneous polarization was determined by the reversal current method [33], the tilt angle by the Clark-Lagerwall method [1] while the switching time as a position of a local maximum in the sample's response to the applied square signal [34].

Broadband dielectric spectroscopy (BDS) measurements were performed using Novocontrol Alpha (Novocontrol Technologies, Germany) dielectric spectrometer with a liquid nitrogen cooling system for the samples of ca. 50 μm thickness between two gold electrodes without aligning layers with a Teflon spacer. Each sample was heated to the isotropic liquid phase and the dielectric spectra were registered on cooling from 393 K to 173 K in the frequency range of 0.1–10<sup>7</sup> Hz. To study the soft mode in the Sm-C\* phase, additional measurements in 40 V external constant bias voltage were performed.

X-ray diffraction (XRD) patterns were registered for the samples in capillaries of borosilicate glass and with the 0.3 mm diameter in a geometry of a horizontal rotating capillary using Empyrean 2 (PANalytical, Netherlands) diffractometer with Cryostream 700 Plus (Oxford Cryosystems, UK) temperature controller. The patterns were collected using CuKα radiation in the  $2\theta = 2-30^\circ$  or  $2-6.5^\circ$  range upon cooling from 393 K to 150 K and on subsequent heating to 298 K. XRD measurement in the room temperature was repeated for each sample after 10 weeks to check for any signs of cold crystallization. Results were analyzed in WinPLOTR [35].

Density functional theory (DFT) calculations were done in Gaussian 16 [36] for isolated molecules in several conformations. The exchange-correlation potential applied was B3LYP [37,38] and the basis set was def2TZVPP [39] together with Grimme's 3D dispersion and Becke-Johnson damping [40,41]. Prior to DFT optimization, preliminary calculations were done with the semi-empirical PM7 method in MOPAC2016 [42,43]. Visualization of molecular models was done by Avogadro [44].

## III. RESULTS AND DISCUSSION

### A. Phase transitions studied by DSC and POM

The DSC curves collected for the W-1000 and W-356 mixtures are presented in Fig. 2. Both mixtures show the same sequence of the smectic phases both during heating and cooling. The small anomalies observed in the high-temperature region for 2 K/min rate (upper insets in Fig. 2) originate from the Iso → Sm-A\* → Sm-C\* → Sm-C<sub>A</sub>\* transitions (in order of descending temperature), which is in agreement with the POM observations (Fig. 3). In the 230–235 K range, the step in the heat flow is observed (bottom insets in Fig. 2), which

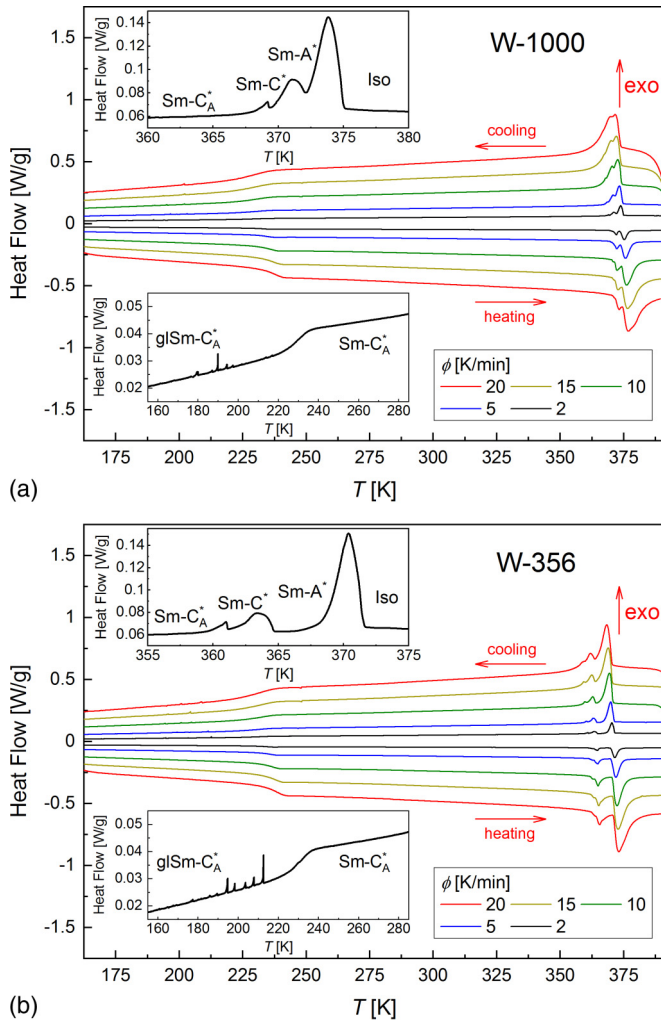
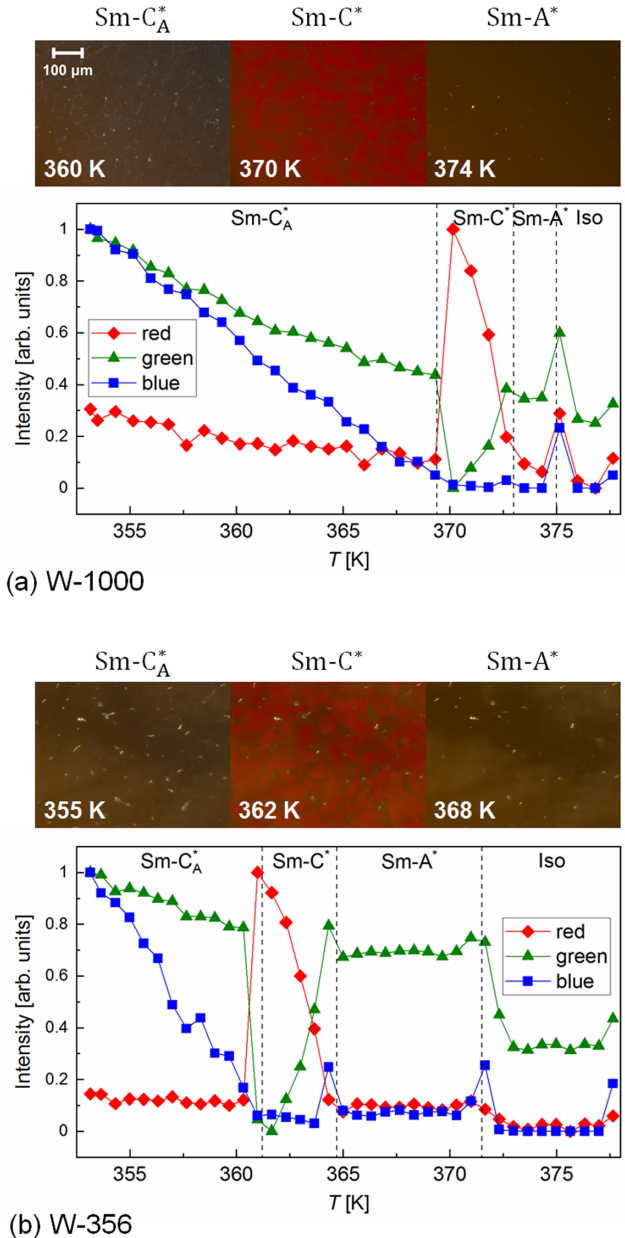


FIG. 2. DSC curves registered during cooling and heating for the W-1000 (a) and W-356 (b) mixtures for several chosen rates. The upper and bottom insets show the temperature region in the vicinity of the clearing temperature and the glass transition, respectively, for 2 K/min cooling rate.

is a sign of the vitrification of the  $Sm-C_A^*$  phase. Several spiky anomalies observed below the glass transition temperature are interpreted as caused by small fractures within the vitrified material [45]. The phase sequence on cooling and heating is the same, and crystallization is not observed. The phase transition temperatures and energy effects are presented in Table II. For the transitions between the smectic and isotropic liquid phase, the onset temperatures of anomalies are given as the phase transition temperatures. The glass transition temperature  $T_g$ , i.e., the vitrification temperature on cooling and the glass softening temperature on heating were determined

TABLE I. Composition of W-1000 and W-356 (weight fractions).

Mixture	3F5HPhF6	3F7FPhH6	C1	C2
W-1000	0.5252	0.4748	–	–
W-356	0.4727	0.4273	0.0570	0.0430



(a) W-1000

(b) W-356

FIG. 3. POM textures of the smectic phases of W-1000 (a) and W-356 (b) registered for unaligned samples during cooling with 2 K/min rate, and the results of the numerical analysis in TOAPy, performed with the “rgb” algorithm. For this option of TOAPy, each pixel is decomposed into red, green and blue contributions denoted by numbers between 0 and 255. Then the normalized sum of each contribution over all pixels is plotted vs temperature [32]. The vertical lines denote the phase transition temperatures determined by DSC for the same cooling rate.

at the half-height of the steps in the DSC curves. The phase transition temperatures are lower and the temperature range of the  $Sm-A^*$  phase is wider for W-356 than for W-1000. The glass transition temperature is only weakly affected by addition of the C1 and C2 components ( $T_g = 229$  K and 232 K for W-1000 and W-356, respectively).

TABLE II. Onset temperatures  $T_o$  and peak temperatures  $T_p$  together with enthalpy  $\Delta H$  and entropy  $\Delta S = \Delta H/T_p$  changes of anomalies in the DSC curves collected for W-1000 and W-356 for 2 K/min rate. Anomalies originating from the  $\text{Sm-C}_A^* \rightarrow \text{Sm-C}^* \rightarrow \text{Sm-A}^*$  transitions on heating were significantly overlapped, therefore only the summed energy effect of these two transitions was determined.

Transition	W-1000				W-356			
	$T_o$ [K]	$T_p$ [K]	$\Delta H$ [kJ/mol]	$\Delta S$ [J/(mol K)]	$T_o$ [K]	$T_p$ [K]	$\Delta H$ [kJ/mol]	$\Delta S$ [J/(mol K)]
Cooling								
Iso $\rightarrow$ Sm-A*	375.0	373.8	4.1	11.0	371.5	370.4	4.5	12.1
Sm-A* $\rightarrow$ Sm-C*	373.0	371.1	1.3	3.6	364.7	363.4	0.9	2.6
Sm-C* $\rightarrow$ Sm-C <sub>A</sub> *	369.4	369.2	0.5	1.4	361.2	361.0	0.4	1.2
Sm-C <sub>A</sub> * $\rightarrow$ glSm-C <sub>A</sub> *	229	–	–	–	232	–	–	–
Heating								
glSm-C <sub>A</sub> * $\rightarrow$ Sm-C <sub>A</sub> *	232	–	–	–	233	–	–	–
Sm-C <sub>A</sub> * $\rightarrow$ Sm-C*	369.9	–	–	–	360.9	362.9	–	–
Sm-C* $\rightarrow$ Sm-A*	370.7	372.1	1.7	4.5	362.6	364.7	1.6	4.3
Sm-A* $\rightarrow$ Iso	373.6	375.3	4.7	12.4	370.0	371.5	4.8	12.8

### B. Electrooptic properties

The monodomains obtained for the studied mixtures are presented in Fig. 4 while the spontaneous polarization, tilt angle of molecules, and switching time are shown in Fig. 5. The C1 and C2 admixtures influence mostly the spontaneous polarization  $P_s$  [Fig. 5(a)]. For W-1000, the spontaneous polarization reaches the maximum value of 225 nC/cm<sup>2</sup>, while for W-356, the  $P_s$  values are smaller by ca. 30 nC/cm<sup>2</sup> in the whole temperature range. The maximum tilt angle  $\Theta$  for W-1000 is 43.1(5)°. It is not the exact  $\Theta = 45^\circ$ , however, it still allows us to classify W-1000 as an orthoconic mixture ( $\Theta = 42^\circ$  is considered enough to obtain desired optical properties for practical purposes [5,46]). For W-356, the average tilt angle is smaller and equal to 40.1(5)° below 323 K, which means that it is not an orthoconic mixture. The first two  $P_s$  values of W-356 (above 362 K, interpreted as originating from the Sm-C\* phase) were not included in further calculations, as it was the case for the last points registered below 304 K and 317 K for W-1000 and W-356, respectively. The dependence of the secondary order parameter  $P_s$  versus the primary order parameter  $\Theta$  is presented in Fig. 5(b). The relationship between these quantities is not linear  $P_s \propto \Theta$  and because of that, the cubic function proposed by Gleeson *et al.* [47] was applied:

$$P_s = \chi_{\perp}(\mu_p \Theta + \mu_{p1} \Theta^3), \quad (1)$$

where  $\chi_{\perp}$  is the transverse dielectric susceptibility and  $\mu_p$ ,  $\mu_{p1}$  are the coupling coefficients. The result of

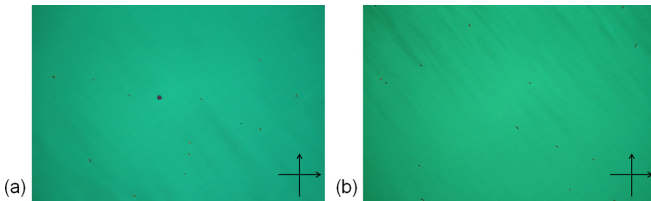


FIG. 4. Monodomains of W-1000 at 368.5 K (a) and W-356 at 361 K (b) in 120 V/4.9 μm field (rectangular signal, 50 Hz, planar alignment). Each texture shows an area of 2.05 × 1.37 mm. The arrows denote the positions of the polarizers.

fitting of Eq. (1) to the experimental  $P_s(\Theta)$  dependence is  $\chi_{\perp} \mu_p = -1.8(4)$  nC/(cm<sup>2</sup>deg) and  $\chi_{\perp} \mu_{p1} = 0.0041(3)$  nC/(cm<sup>2</sup>deg<sup>3</sup>) for W-1000. For W-356, the coupling between  $P_s$  and  $\Theta$  is weaker, as the coefficient  $\chi_{\perp} \mu_p$  is zero within uncertainty and  $\chi_{\perp} \mu_{p1} = 0.0029(2)$  nC/(cm<sup>2</sup>deg<sup>3</sup>).

The relationship between the switching time  $\tau_{sw}$  of W-1000 and W-356 is different for different temperature ranges [Fig. 5(c)]. Above 350 K, the switching time is shorter for W-356 than for W-1000. In the 335–350 K range, the  $\tau_{sw}$  values are basically the same for both mixtures, and below 335 K the switching time in W-356 becomes longer than for W-1000 but even in the lowest studied temperature, 283 K, the longest  $\tau_{sw}$  is small and equal to 1.460(5) ms and 1.77(1) ms for W-1000 and W-356, respectively. Values of  $\tau_{sw}$  and  $P_s$  were used to calculate the rotational viscosity from the

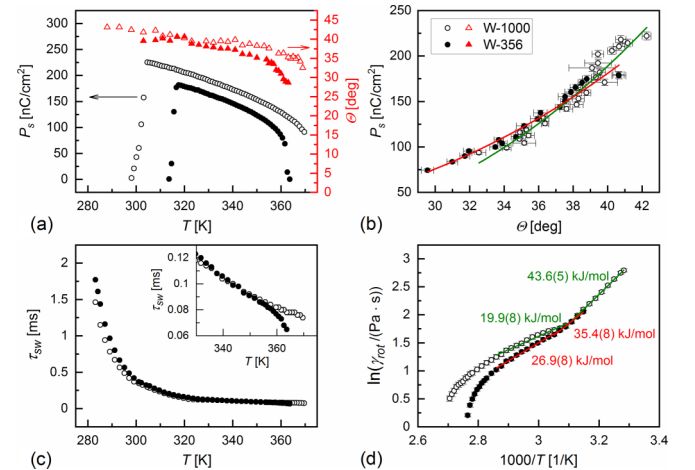


FIG. 5. Electrooptic parameters of the W-1000 (open symbols) and W-356 (solid symbols) mixtures: spontaneous polarization  $P_s$  and tilt angle  $\Theta$  (a), coupling between  $P_s$  and  $\Theta$  in the Sm-C<sub>A</sub>\* phase with fitting results of Eq. (1) (b), switching time  $\tau_{sw}$  (c), as well as the Arrhenius plot of the rotational viscosity  $\gamma_{rot}$  of the Sm-C<sub>A</sub>\* phase (d). The inset in panel (c) shows the  $\tau_{sw}$  values close to the Sm-A\*/Sm-C\* transition. The legend in panel (b) applies to the whole figure.

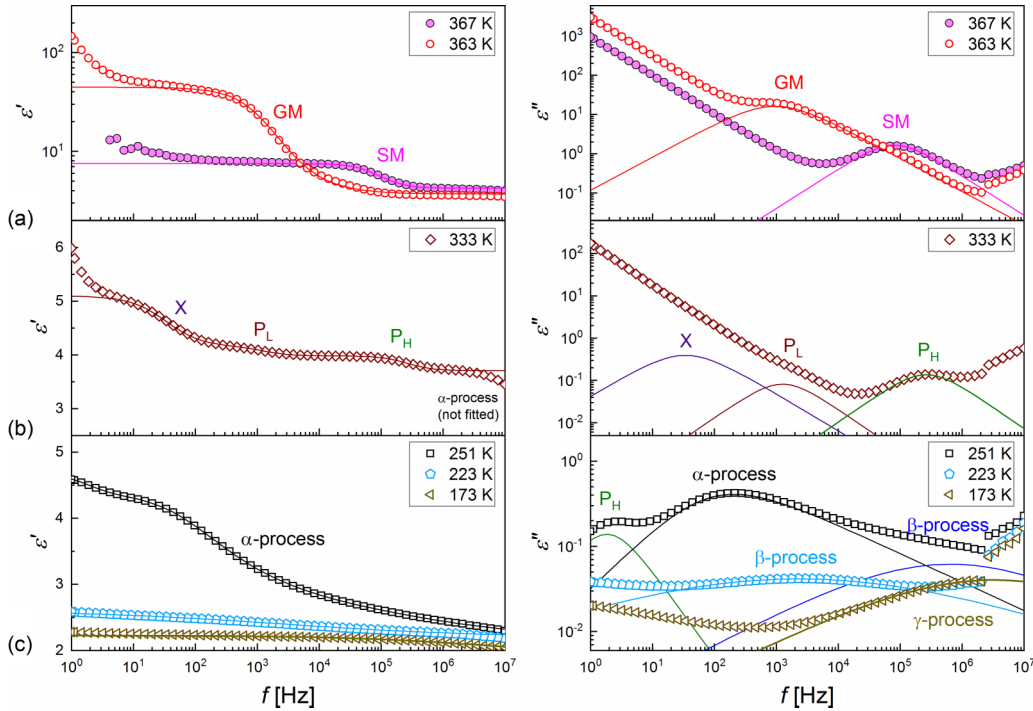


FIG. 6. Dielectric dispersion (right side) and absorption (left side) of W-356 in the Sm-A\*, Sm-C\* (a) and Sm-C<sub>A</sub>\* (b), (c) phases. Fitting results of Eq. (3) are marked by lines, separately for each relaxation process (ionic conductivity and electrode capacity parts are omitted). The spectrum for the Sm-A\* phase at 367 K was registered in the 0.8 V/μm bias field, while other presented spectra were collected without the bias field. All spectra were registered on cooling.

formula [48,49]:

$$\gamma_{\text{rot}} = \tau_{\text{sw}} P_s E, \quad (2)$$

where  $E$  is the amplitude of an applied electric field (24.5 V/μm in this study). Above 350 K, the temperature dependence of  $\gamma_{\text{rot}}$  does not follow the Arrhenius formula [Fig. 5(d)] and the activation energy  $E_{\text{rot}}$  for collective reorientation on the tilt cone cannot be determined. For W-1000 below 350 K, two regions of linear dependence, characterized by two different  $E_{\text{rot}}$  values, are visible. In the 324–350 K range, the activation energy is equal to  $E_{\text{rot}} = 19.9(8)$  kJ/mol. In the lower-temperature range of 299–324 K the activation energy is twice as large,  $E_{\text{rot}} = 43.6(5)$  kJ/mol. Similar situation occurs for W-356, although the change of the slope in the Arrhenius plot is observed at slightly higher temperature (328 K), and the difference in the activation energy is smaller than for W-1000. The  $E_{\text{rot}}$  values obtained in the 328–350 K and 314–328 K ranges for W-356 are 26.9(8) and 35.4(8) kJ/mol, respectively. Noteworthy, the region around 325 K, where the  $E_{\text{rot}}(T)$  dependence changes, is also the temperature below which the tilt angle does not change on cooling as significantly as in higher temperatures, especially in W-356 [Fig. 5(a)]. It implies that the change in the temperature dependence of the rotational viscosity is caused by some structural changes within the Sm-C<sub>A</sub>\* phase.

### C. Molecular dynamics investigated by BDS

The dielectric spectra were analyzed with the Havriliak-Negami formula [50] of the complex permittivity:

$$\varepsilon^*(f) = \varepsilon_{\infty} + \sum_j \frac{\Delta\varepsilon_j}{[1 + (2\pi i f \tau_j)^{1-\alpha_j}]^{\beta_j}} - \frac{i\sigma}{2\pi f \varepsilon_0} + \frac{C}{f^{1.5}}, \quad (3)$$

where  $\varepsilon_{\infty}$  is the permittivity in the high-frequency limit,  $\Delta\varepsilon_j$  is the dielectric increment,  $\tau_j$  is the relaxation time, and  $\alpha_j$  and  $\beta_j$  are parameters describing the width and asymmetry of the distribution of the relaxation time of the  $j$ th process, respectively. For  $\beta_j = 1$ , the Havriliak-Negami model transforms into the Cole-Cole model, which assumes the symmetric distribution of relaxation times [51]. The third and fourth terms apply, respectively, to the low-frequency background originating from the ionic conductivity  $\sigma$  of a substance and the capacitance of electrodes [52].

The representative dielectric spectra together with the fitting results of Eq. (3) for the W-356 mixture are shown in Fig. 6. The Arrhenius plots of the relaxation time of all processes registered for the W-1000 and W-356 mixtures are presented in Fig. 7(a) and the dielectric strength of each process is shown in Fig. 7(b). Addition of the C1 and C2 compounds to W-1000, leading to the W-356 mixture, does not cause dramatic changes in the dielectric relaxation processes. The soft mode (SM), i.e., the collective fluctuations of the tilt angle, can be identified by increasing of the relaxation time and dielectric strength as the temperature decreases in the Sm-A\* phase and subsequent decreasing of these quantities in the Sm-C\* phase [53,54]. The second relaxation process present

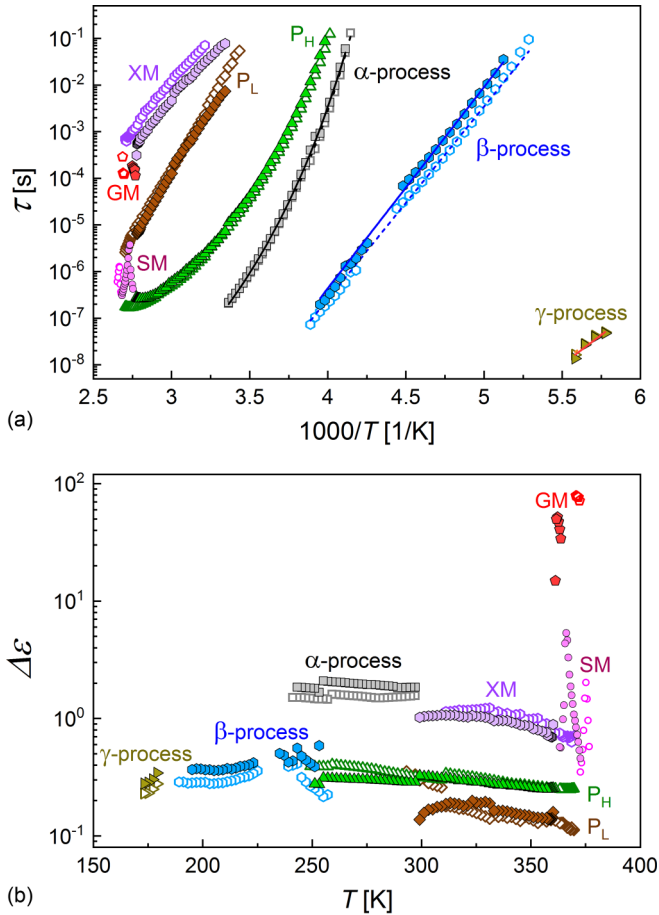


FIG. 7. Arrhenius plot of the relaxation time (a) and temperature dependence of the dielectric strength (b) of relaxation processes observed in W-1000 (open symbols) and W-356 (solid symbols). Results for the soft mode were obtained in the 0.8 V/ $\mu$ m bias field.

in the Sm-C\* phase was interpreted as the Goldstone mode (GM), i.e., the collective fluctuations of molecules around the cone, which is characterized by the largest dielectric strength among all observed processes [Fig. 6(a)], and which can be suppressed by the bias field [53,54] (see Fig. S1 in the Supplemental Material (SM) [55]). Below the Sm-C\*<sub>A</sub> → Sm-C\* transition, three relaxation processes are visible, denoted here as X,  $P_L$ , and  $P_H$  [Fig. 6(b)]. It is known from the previous studies that for another modification of W-1000 as well as for one of its components (3F5HPhF6) two relaxation processes can be identified as  $P_L$  and  $P_H$  phasons [18,27], originating from the in-phase and antiphase collective movements of molecules from the neighboring smectic layers around the cone, respectively [56]. The X-mode, with the lowest frequency, and similar relaxation time to the Goldstone mode close to the Sm-C\* → Sm-C\*<sub>A</sub> transition [Fig. 7(a)] could be interpreted as a hereditary Goldstone mode, caused by the small preserved domains of the Sm-C\* phase, coexisting with the Sm-C\*<sub>A</sub> phase [57]. However, in the POM results (Fig. 3) the coexistence of the Sm-C\* and Sm-C\*<sub>A</sub> phases is not observed in a wide temperature range. It means that the more likely explanation of the X-mode are relaxations at the liquid crystal/electrode interface [58–62].

Two other processes appear in the measured frequency range with further cooling [Fig. 6(c)]: the  $\alpha$  process and the secondary  $\beta$  process. The  $\alpha$  process is characterized by a significantly asymmetric distribution of the relaxation time. The width of the distribution increases with decreasing temperature: the Cole-Cole parameter  $\alpha_\alpha$  is equal to 0.10–0.15 above 260 K and it increases to 0.3–0.4 at 243–245 K. The  $\beta_\alpha$  parameter of the Havriliak-Negami distribution is equal to 0.3–0.35 above 260 K and it decreases slightly with decreasing temperature, but at lower temperatures,  $\beta_\alpha$  increases up to 0.5–0.6 at 243–245 K, which means that the shape of the dielectric loss peak becomes more symmetrical. The shape parameters of the Havriliak-Negami model apply to the distribution of the relaxation time, however, there is another interpretation of the shape of the dielectric loss peak proposed by Jonscher [63]. The slope of the high-frequency side of the  $\ln \epsilon''(\ln 2\pi f)$  peak decreases with increasing short-range correlations, and the slope of the low-frequency side increases with increasing long-range interactions [63]. The high-frequency slope  $n_{HF}$  and low-frequency slope  $n_{LF}$  are related to the Havriliak-Negami shape parameters by formulas  $n_{HF} = (1 - \alpha)\beta$  and  $n_{LF} = 1 - \alpha$  [64]. For the  $\alpha$ -process above 260 K,  $n_{HF} = 0.25$ –0.3 and  $n_{LF} = 0.85$ –0.9. At 243–245 K,  $n_{HF}$  increases only to 0.3–0.35, whereas  $n_{LF}$  decreases to 0.6–0.7. This result implies the slight decrease of short-range correlations and decrease of long-range correlations in the Sm-C\*<sub>A</sub> phase with decreasing temperature. This is an interesting result, since upon approaching the glass transition, one would expect the increase of short-range correlations [64]. It can be explained by the presence of the underlying  $\beta$ -process above 253–257 K, which is too overlapped with the  $\alpha$ -process to be included in fitting but which leads to the underestimation of  $n_{HF}$  of the  $\alpha$ -process. It is confirmed by steps in the  $n_{HF}(T)$  and  $n_{LF}(T)$  dependencies when the  $\beta$ -process is included in fitting (Fig. S2 in SM). Noteworthy, the change of the fitting model does not lead to any significant discontinuities in the  $\tau_\alpha(T)$  dependence.

The origin of the  $\alpha$ -process in the liquid crystalline substances is still not clear. For the 5P-EtFLET-P5 [64] and 4CFPB [65] compounds exhibiting the vitrified nematic phase, the  $\alpha$ -process is explained as related to rotations around the short molecular axis (precisely, the axis of the largest moment of inertia), named the s-process. Such interpretation was applied also for the smectogenic BBOA [66], 3F3HPhF6 [67], and 3F5FPhF6 [68] compounds. However, in another study [57] the existence of an underlying relaxation process at similar frequency as the  $P_L$  phason is proved. The underlying process is interpreted as the s-process, which means that the  $\alpha$ -process, with much higher frequency, is rather the collective version of the l-process - rotations around the long molecular axis (axis of the smallest moment of inertia). Also for nematogenic 5CB [69] and smectogenic 3F7HPhH7 [70] the  $\alpha$ -process is interpreted as related to the l-process. Regardless of the exact origin of the  $\alpha$ -process observed in the Sm-C\*<sub>A</sub> phase, it is a collective process [62,71], which differs from molecular processes s and l observed in nonglass-forming liquid crystals, with the relaxation time decreasing with increasing temperature according to the Arrhenius formula. The relaxation time of the  $\alpha$ -process,  $\tau_\alpha$ , changes with temperature according to the Vogel-Fulcher-Tammann (VFT)

TABLE III. Fitting parameters of the VFT formula for the  $\alpha$ -process and the Arrhenius formula for the  $\beta$ - and  $\gamma$ -process in the W-1000 and W-356 mixtures. The glass transition temperature and fragility parameter obtained from the VFT parameters are also given.

$\alpha$ -process	W-1000	W-356
$\tau_0$ [s]	$1.1(3) 10^{-12}$	$2.0(1.1) 10^{-12}$
$B$ [K]	1307(35)	1574 (81)
$T_V$ [K]	189.7(8)	183(2)
$T_g$ [K]	230.3(1)	229.7(3)
$m_f$	79.1(9)	73(2)
$\beta$ -process		
$\tau_0$ [s]	$7.5(3.7) 10^{-24}$	$2.4(1.2) 10^{-24}$
$E_a$ [kJ/mol]	79.1(8)	82.6(8)
$\gamma$ -process		
$\tau_0$ [s]	$0.2(1.1) 10^{-20}$	$1.0(6.2) 10^{-22}$
$E_a$ [kJ/mol]	44.3(6.7)	48.7(8.0)

equation [62]:

$$\tau_\alpha(T) = \tau_0 \exp\left(\frac{B}{T - T_V}\right), \quad (4)$$

where  $\tau_\infty$  is the pre-exponential constant,  $T_V$  is the Vogel temperature ( $\tau_\alpha(T_V) \rightarrow \infty$ ) and  $B$  is a constant that equals an activation energy if  $T_V = 0$ . The parameters of the VFT equation are connected with the fragility index  $m_f$ , which is defined as [72]

$$m_f = \left. \frac{d \log_{10} \tau_\alpha(T)}{d(T_g/T)} \right|_{T_g}, \quad (5)$$

where  $T_g$  is the glass transition temperature, where  $\tau_\alpha = 100$  s. Combination of Eqs. (4) and (5) gives an alternate formula for the fragility index:

$$m_f = \frac{BT_g}{(T_g - T_V)^2 \ln 10}. \quad (6)$$

The fitting results of the VFT formula to the  $\tau_\alpha(T)$  dependence for the W-1000 and W-356 mixtures are collected in Table III. The fragility index determined by BDS is  $m_f = 79.1(9)$  for W-1000 and  $m_f = 73(2)$  for W-356. Therefore, the addition of the C1 and C2 components to the W-1000 mixture leads to decrease of the fragility, which, consequently, decreases probability of cold crystallization [73] in the W-356 mixture, as compared to W-1000. Both W-1000 and W-356 mixtures are stronger glassformers than most of the investigated previously pure chiral smectogenic compounds from the 3FmX<sub>1</sub>PhX<sub>2</sub>r family, which fragilities are  $m_f = 136$ , 150 for 3F7HPhH7 (double  $\alpha$ -process) [70],  $m_f = 102$  for 3F7HPhF6 [74],  $m_f = 89$  for 3F5HPhH6 [75], and  $m_f = 72$  for 3F7HPhH6 [76]. We did not find any experimental reports regarding the fragilities of mixtures including similar compounds as these used in W-1000 and W-356. The fragilities of the pure main components of the studied mixtures, namely 3F5HPhF6 and 3F7HPhH6, will be reported in future publications.

In the high-frequency tail of the  $\alpha$ -process, the weaker, secondary  $\beta$ -process is observed [Fig. 6(c)]. The frequency of this process decreases with decreasing temperature slower

than for the  $\alpha$ -process, therefore below 230 K these relaxation processes are well-separated. The  $\beta$ -process is characterized by the very wide, symmetric distribution of the relaxation time. In the 230–260 K range, the Cole-Cole parameter  $\alpha_\beta$  increases with decreasing temperature from 0.5 to 0.75 for W-1000, while for W-356 it takes values from the 0.6–0.75 range without any monotonous temperature dependence. Below 230 K,  $\alpha_\beta = 0.7$ –0.8 for both mixtures. Such high value of  $\alpha_\beta$  means, according to Jonscher's interpretation [63], that the  $\beta$ -process is related mainly to short-range correlations within material. The relaxation time  $\tau_\beta$  of the  $\beta$ -process follows the Arrhenius dependence [Fig. 7(a)]. The determined activation energy values are  $E_a = 79.1(8)$  kJ/mol for W-1000 and 82.6(8) kJ/mol for W-356. The question is whether the  $\beta$ -process in the vitrified Sm-C<sub>A</sub>\* phase of W-1000 and W-356 is a genuine Johari-Goldstein (JG) process, arising from the movements of the whole molecules [77]. The investigated mixtures do not consist of rigid molecules, therefore the  $\beta$ -process can also originate from intramolecular motions [70,71,78]. For the genuine JG process, the relationship between parameters of the  $\alpha$ -process and  $\beta$ -process was derived to be [79]

$$\frac{E_a}{RT_g} = 2.303(2 - 13.7n' - \log_{10} \tau_0). \quad (7)$$

Parameters  $E_a$  and  $\tau_0$  are the activation energy and pre-exponential factor in the Arrhenius dependence of  $\tau_\beta(T)$  of the  $\beta$ -process (Table III), while  $n'$  is the parameter of the Kohlrausch-Williams-Watts (KWW) relaxation function  $\phi(t) = \exp[-(t/\tau_\alpha)^{1-n'}]$  [80] describing the  $\alpha$ -process. The KWW function is in the time domain, however, the value of  $n'$  may be estimated from the parameters of the Havriliak-Negami model using the formula given by Alvarez *et al.* [81],  $(1 - \alpha)\beta = (n')^{1.23}$ . For both mixtures,  $n' \approx 0.42$  is obtained. The  $E_a/RT_g$  value is equal to 41.2 for W-1000 and 38.2 for W-356, while the right-hand side of Eq. (7) is in both cases higher, 44.8 and 45.2 for W-1000 and W-356, respectively. Such small difference does not allow to claim unambiguously that the  $\beta$ -process in the investigated mixtures is not the genuine JG process, especially that the value of  $n'$  is only an estimation. However, when one takes into account numerous possible rotations around bonds within the considered molecules, the  $\beta$ -process is more probably a pseudo-JG relaxation and it originates in this case rather from intramolecular rotations.

The highest-frequency one among observed relaxation processes, denoted as the  $\gamma$ -process, enters the investigated frequency range close to 173 K, the lowest temperature achievable in the used experimental setup. Since the fitting of Eq. (3) was possible for the  $\gamma$ -process only in a few last registered BDS spectra (with the symmetric distribution assumed), the uncertainties of the fitting parameters of the Arrhenius formula are considerable and  $\tau_0$  cannot be determined (Table III), however, it is possible to estimate the activation energy of the  $\gamma$ -process as 45–50 kJ/mol. As it can be seen in the Arrhenius plot [Fig. 7(a)], the relaxation times of this secondary process are over one order of magnitude smaller than these for the  $\beta$ -process and its activation energy is also smaller, indicating that the  $\gamma$ -process is caused by conformational changes within molecules. The further interpretation of the relaxation

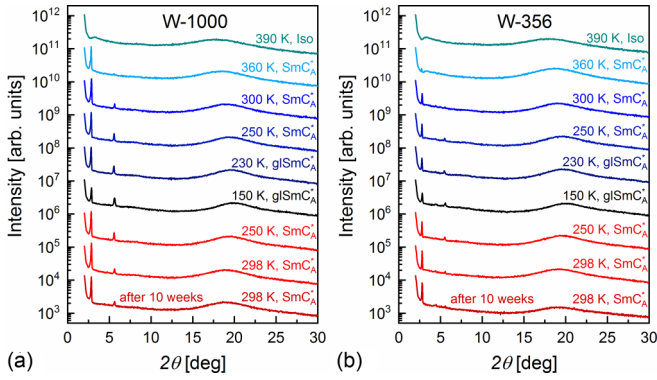


FIG. 8. X-ray diffraction patterns of W-1000 (a) and W-356 (b) collected on cooling from 390 K to 150 K and subsequent heating to 298 K. The intensity is shown in the logarithmic scale.

processes observed below the room temperature is based on the DFT calculations, which are presented in Sec. III E.

#### D. Structural parameters studied by XRD

The x-ray diffraction patterns of the Sm-A<sup>\*</sup>, Sm-C<sup>\*</sup>, and Sm-C<sub>A</sub><sup>\*</sup> phases are similar, as these phases possess the same basic structural features: (1) quasi-long-range layer order and (2) short-range order within the smectic layers. The former corresponds to the sharp peak appearing at low  $2\theta$  values and the latter corresponds to the diffuse maximum appearing at higher angles, observed also for the isotropic liquid [82]. There is no low-angle sharp peak visible in the XRD patterns of W-1000 and W-356 (Fig. 8) collected for isotropic liquid (390 K). For W-1000 [Figs. 8(a) and 9(a)], the peak at  $2\theta = 2.6^\circ$  arises at 375 K, which is in agreement with the Iso  $\rightarrow$  Sm-A<sup>\*</sup> transition temperature determined by DSC and POM. Its intensity increases initially with decreasing temperature.

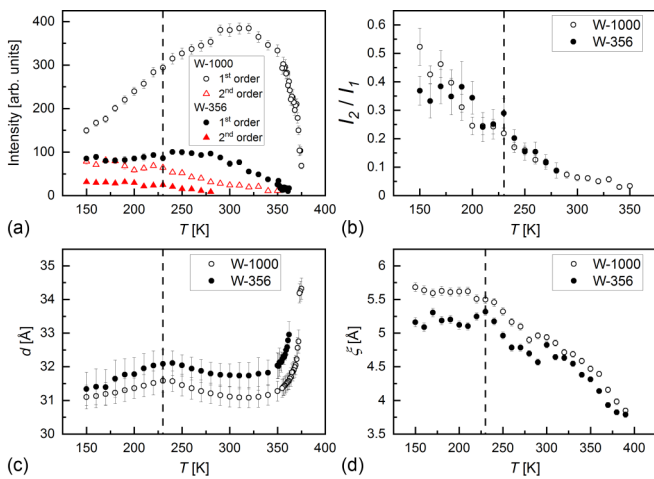


FIG. 9. Integrated intensities of diffraction peaks arising from the smectic layer order (a), the ratio of integrated intensities of the second- and first-order peaks (b), smectic layer spacing (c), and correlation length of the intralayer short-range order (d) vs temperature determined from the diffraction patterns of W-1000 and W-356. The vertical line in each panel shows the glass transition temperature determined by DSC.

At 350 K, well below the Sm-C<sup>\*</sup>  $\rightarrow$  Sm-C<sub>A</sub><sup>\*</sup> transition, the second-order peak at  $2\theta = 5.6^\circ$  appears. The intensity of the second-order peak increases on cooling down to 150 K, the lowest studied temperature, while for the first-order peak, the maximal intensity is reached around the room temperature and on further cooling the decrease of intensity is observed. For W-356, the low-angle peak appears at ca. 360 K, which is already within the Sm-C<sub>A</sub><sup>\*</sup> phase, and its intensity is much lower than for W-1000 [Figs. 8(b) and 9(a)]. The second-order peak becomes also visible at lower temperature, at ca. 280 K. The possible explanation is the larger number of defects in the smectic layers in W-356 compared to W-1000, which consequently leads to the significant decrease of the intensity of the diffraction peaks arising from the layer order. It is in agreement with the POM observations, because textures for W-1000 are more homogeneous than for W-356 (Fig. 3). Similar absence of the low-angle peak, probably due to numerous defects, was observed for the two-component mixture (80% 3F5FPhF6 and 20% 3F7HPhF6) doped with BaTiO<sub>3</sub> nanoparticles [83].

Although the absolute intensities are different, the temperature dependence of the ratio of intensities of the second- and first-order peaks [denoted as  $I_2/I_1$ , Fig. 9(b)] is similar for W-1000 and W-356. The  $I_2/I_1$  ratio is proportional to the  $\eta_2^2/\eta_1^2$  value, where  $\eta_1$ ,  $\eta_2$  are the first and second smectic layer order parameters, respectively [84]. After an appearance of the second-order peak at  $2\theta = 5.6^\circ$ , the  $I_2/I_1$  ratio increases on cooling and at 150 K it is equal to 0.55 and 0.35 for W-1000 and W-356, respectively. The increase of  $I_2/I_1$  indicates the increase of  $\eta_2^2/\eta_1^2$ , which means that the modulation of the electron density along the smectic layer normal deviates from the simple sinusoidal dependence (for which  $\eta_2 = 0$ ) with decreasing temperature [84]. In the 170–280 K range, the increase of  $I_2/I_1$  is approximately linear in W-1000, with no distinct indication of the glass transition. For W-356, there is a small anomaly in the temperature dependence of  $I_2/I_1$  at 230 K, although it is on the brink of the experimental error. Also the  $I_2/I_1$  ratio does not reach as high value as for W-1000. However, the evolution of the smectic layer order in W-356 is well visible as the change of the full-width at half-height (FWHM) of the diffraction peak at  $2\theta = 2.9^\circ$ . At the glass transition of the Sm-C<sub>A</sub><sup>\*</sup> phase,  $\text{FWHM} = 0.072(6)^\circ$  and it increases to  $0.089(8)^\circ$  with decreasing temperature down to 150 K (Fig. S3 in SM). The widening of the low-angle diffraction peak suggests the decrease of the quasi-long-range order in the vitrified Sm-C<sub>A</sub><sup>\*</sup> phase of W-356 [82].

The smectic layer spacing  $d$  [Fig. 9(c)] was determined from the low-angle peak position ( $2\theta = 2.6 - 2.9^\circ$ ) by the Bragg equation  $d = \lambda/(2 \sin \theta_d)$ , where  $\lambda$  is the x-ray wavelength and  $\theta_d$  is the peak position [82]. For W-1000, the layer spacing shows a discontinuous drop from  $34.2(3) \text{ \AA}$  to  $32.8(4) \text{ \AA}$  between 373 and 372 K, indicating the Sm-A<sup>\*</sup>  $\rightarrow$  Sm-C<sup>\*</sup> transition. For W-356, the layer spacing in the Sm-A<sup>\*</sup> and Sm-C<sup>\*</sup> phases cannot be determined as the low-angle peak is not visible. Within the temperature range of the Sm-C<sub>A</sub><sup>\*</sup> phase, the layer spacing shows the same qualitative temperature dependence in both mixtures, although it is larger in W-356 than in W-1000, with the difference decreasing with decreasing temperature from almost  $1.4 \text{ \AA}$  at 362 K to only  $0.2\text{--}0.3 \text{ \AA}$  at 150–170 K. On cooling down to 350 K, the



layer spacing decreases rapidly and then, from 350 K down to the room temperature, it reaches a shallow minimum. Below 290–300 K, the  $d$  value increases slowly on cooling until the glass transition temperature. The minimum in  $d$  around 300–320 K overlaps with the onset of faster increasing of the  $I_2/I_1$  ratio with decreasing temperature for W-1000 and appearance of the second-order peak for W-356. The apparent structural changes in the  $\text{Sm-C}_A^*$  phase that occur in that temperature range seem to be correlated with the change of the slope in the Arrhenius plot of the rotational viscosity [Fig. 5(d)]. At the glass transition temperature,  $T_g = 230\text{--}240$  K, the temperature dependence is reversed and within the vitrified  $\text{Sm-C}_A^*$  phase the layer spacing decreases on cooling. The changes in  $d$  are within uncertainty bars, however, uncertainty values presented in Fig. 9(c) are based on the half-width of the diffraction peak, while uncertainties of the peak position obtained from fitting of the pseudo-Voigt function are more than one order of magnitude smaller.

At the closer look at the low-angle region of the XRD patterns of the  $\text{Sm-C}_A^*$  phase of W-356, one can see an additional, weak peak at  $2\theta = 4.4^\circ$  between the first- and second-order peaks from the smectic layers [see Fig. 8(b) and Fig. S3 in SM]. The presence of this peak is caused supposedly by modulation of the smectic layer structure in a plane perpendicular to the smectic layers. The possible model, presented in Fig. S3, assumes the primitive two-dimensional rectangular “unit cell” with  $a = d \approx 31$  Å and  $b \approx 26$  Å. The first and second diffraction peaks from the smectic layer order are then the (10) and (20) peaks, respectively, and the additional peak at  $2\theta = 4.4^\circ$  can be indexed as the (11) peak.

Parameters characterizing the short-range positional order in the isotropic liquid in three dimensions and in the smectic layers in two dimensions are the average distance  $d_{\text{SRO}}$  between molecules and the correlation length  $\xi$ . Both can be determined by fitting to the diffuse maximum at  $2\theta = 18^\circ$  the Lorentz peak function  $I(q) = 1/(1 + \xi^2(q - 2\pi/d_\perp)^2)$ , where  $q = 4\pi \sin \theta/\lambda$  is the length of the scattering vector [82]. The  $d_{\text{SRO}}$  values (not shown) are within the 4.5–5.0 Å range, decreasing with decreasing temperature. The correlation length [Fig. 9(d)] is equal to ca. 3.7 Å starting from 390 K, and within the smectic phases it increases linearly with decreasing temperature. Below  $T_g = 230$  K, the correlation length stabilizes at 5.5–5.7 Å for W-1000 and 5.0–5.3 Å for W-356. An almost constant  $\xi$  parameter in the vitrified  $\text{Sm-C}_A^*$  phase was observed also for pure 3FmHPhF6 ( $m = 5\text{--}7$ ) homologues [27,74]. The overall XRD results imply that below the glass transition temperature, the short-range order in two dimensions within the smectic phases does not evolve, while the quasi-long-range lamellar order in the third dimension still changes.

After cooling the sample down to 150 K, the diffraction patterns were registered on heating at 200, 225, 250, 275, and 298 K. Representative patterns for 250 and 298 K (Fig. 8) show that both mixtures are still in the  $\text{Sm-C}_A^*$  phase and the signs of cold crystallization are not visible. The crystal phase of 3F5HPhF6, one of the components of W-1000 and W-356, melts at 301 K [26], therefore the probability of crystallization of the investigated mixtures at the room temperature is very small. The patterns collected at the room temperature 10 weeks after heating the sample from 150 K (at the bottom of

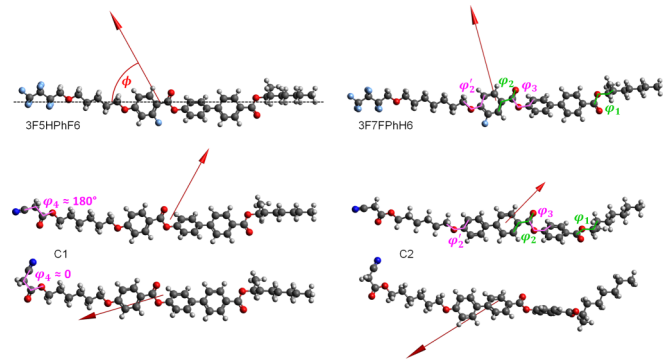


FIG. 10. Molecules of the components of the W-1000 and W-356 mixtures, optimized with the DFT-B3LYP/def2TZVPP method in conformations with the lowest conformational energy for considered torsional angles ( $\varphi_1 \approx 276^\circ$ ,  $\varphi_2 \approx 180^\circ$ ,  $\varphi'_1 \approx 0$ ,  $\varphi_3 \approx 303\text{--}306^\circ$ ,  $\varphi_4 \approx 180^\circ$  or  $0^\circ$ ). The arrows indicate the total dipole moment vectors  $\vec{\mu}$  and  $\phi$  is an angle between  $\vec{\mu}$  and the molecular long axis (shown for 3F5HPhF6 by the dashed line).

Fig. 8) prove that W-1000 and W-356 remain in the  $\text{Sm-C}_A^*$  phase.

### E. Molecular modeling

Molecular modeling was performed for isolated molecules of the W-1000 and W-356 components in various conformations (Fig. 10). The conformational energy calculations were done for several torsional angles: C-O-C\* (denoted as  $\varphi_1$ ) as well as C-C-C=O ( $\varphi_2$ ) and C-O-C-C ( $\varphi_3$ ) next to the C=O group between the benzene ring and biphenyl, and C-O-C-C ( $\varphi'_2$ ) on the other side of the benzene ring. For the C1 and C2 molecules, the conformational energy scans were done also for the (N ≡ C)-C-C-O torsional angle denoted as  $\varphi_4$ . We chose such torsional angles which change preserves the hockey-stick shape of molecules. Afterwards, for each local minimum and maximum in relative conformational energy, the DFT-B3LYP/def2TZVPP calculations were performed to obtain more reliable values of energy barriers for intramolecular rotations (Fig. 11). For the  $\varphi_2$  and  $\varphi'_2$  angles, the calculations were done simultaneously with the condition  $\varphi_2 + \varphi'_2 = 180^\circ$  to calculate the energy barrier for rotation of the benzene ring (or biphenyl for C2). The energy barriers determined by the DFT calculations are in most of cases larger than values obtained by the faster PM7 method. Moreover, PM7 does not reproduce the local minimum of the conformational energy for  $\varphi'_4 \approx 180^\circ$ , which one can see in the DFT results [Fig. 11(d)].

The total dipole moment  $\mu$  of a molecule and the angle  $\phi$  between the  $\vec{\mu}$  vector and the molecular long axis (calculated by linear regression of the atom coordinates weighted by the atomic mass, Fig. 10) are sensitive to the conformation of 3F5HPhF6, 3F7FPhH6, C1, and C2 molecules (see Table S1 in SM). The changes in  $\varphi_3$  and  $\varphi_4$  angles lead to the most significant changes in the dipole moment and they are also characterized by the smallest energy barriers for intramolecular rotations, therefore they were chosen to calculate the average dipole moment. In further discussion, the transverse component  $\mu_\perp = \mu \sin \phi$  of the dipole moment

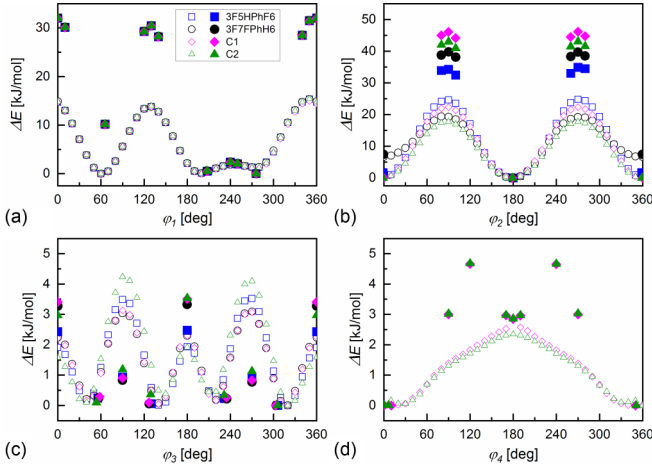


FIG. 11. Relative conformational energy, with respect to the lowest-energy conformation for each torsional angle and compound, calculated with the PM7 (open symbols) and DFT-B3LYP/def2TZVPP (solid symbols) methods for torsional angles  $\varphi_1, \varphi_2$  ( $\varphi'_1 = 180^\circ - \varphi_2$ ),  $\varphi_3, \varphi_4$  indicated in FIG. 10.

will be considered because only this component contributes to the total spontaneous polarization. The average transverse dipole moment  $\langle \mu_\perp \rangle$  for each component was obtained as the Boltzmann average over local minima in conformational energies related to the change of  $\varphi_3$  and  $\varphi_4$  angles:

$$\langle \mu_\perp \rangle = \frac{\sum_\varphi \mu_\perp \exp\left(\frac{-\Delta E_\varphi}{RT}\right)}{\sum_\varphi \exp\left(\frac{-\Delta E_\varphi}{RT}\right)}, \quad (8)$$

where  $\Delta E_\varphi$  and  $\mu_\perp$  are, respectively, the relative conformational energy and transverse dipole moment for a molecular conformation in each energy minimum,  $R$  is the gas constant and  $T = 300$  K. Calculations for  $T = 200$  K and 400 K show that the Boltzmann average is almost temperature independent in the 200–400 K range. The calculated  $\langle \mu_\perp \rangle$  values are shown in Table IV. For the 3F5HPhF6 and 3F7FPhH6 compounds, the average transverse dipole moment is ca. 2.4 D and 2.7 D, respectively, which consequently gives  $\langle \mu_\perp \rangle = 2.55$  D for W-1000. For C1 and C2 compounds present only in W-356,  $\langle \mu_\perp \rangle \approx 2$  D when only fully extended conformations,

TABLE IV. Average transverse dipole moments (in debye) of the W-1000 and W-356 mixtures and their components, calculated as the Boltzmann averages in 300 K over conformations in the local minima in the  $\Delta E(\varphi_3)$  and  $\Delta E(\varphi_4)$  dependencies. The relative conformational energies and  $\mu_\perp$  values for each conformation were obtained by the DFT-B3LYP/def2TZVPP calculations, with torsional angles  $\varphi_1 \approx 276^\circ$  and  $\varphi_2 \approx 180^\circ$ .

Component	$\langle \mu_\perp(\varphi_3) \rangle$	$\langle \mu_\perp(\varphi_3, \varphi_4) \rangle$
3F5HPhF6	2.38	—
3F7FPhH6	2.75	—
C1	1.96	2.99
C2	1.98	3.08
W-1000	2.55	—
W-356	2.48	2.61

i.e., with  $\varphi_4 \approx 180^\circ$  are included in averaging. The  $\langle \mu_\perp \rangle$  value for the W-356 mixture is then equal to  $\langle \mu_\perp \rangle = 2.48$  D, slightly lower than for W-1000, which is in agreement with a lower spontaneous polarization obtained for W-356 [Fig. 5(a)]. However, molecular modeling results show that for the C1 and C2 molecules, the conformations with the bend ( $\text{N} \equiv \text{C}$ )-C-C-O chain ( $\varphi_4 \approx 0^\circ$ ) are characterized by lower conformational energies and in most cases by larger transverse dipole moments than the fully extended ones. When one includes both conformations with  $\varphi_4 \approx 180^\circ$  and  $\varphi_4 \approx 0^\circ$  in calculations of the Boltzmann average, one obtains  $\langle \mu_\perp \rangle \approx 3$  D for C1 and C2 and  $\langle \mu_\perp \rangle = 2.61$  D for the W-356 mixture. Such result suggests that the spontaneous polarization is expected to be larger in W-356 than in W-1000, which is in discrepancy with the experimental data. The possible explanation is that in the real mixture, the C1 and C2 molecules take conformations mostly with the extended ( $\text{N} \equiv \text{C}$ )-C-C-O chain. Although bending of the ( $\text{N} \equiv \text{C}$ )-C-C-O chain leads to decrease of the conformational energy for isolated C1 and C2 molecules, it can be hindered by steric interactions within the smectic layer, when the average distance between the long axes of molecules is  $d_{\text{SRO}} \approx 4.7$  Å, as determined from the XRD patterns. Even when only extended conformations are considered, the calculated average transverse dipole moment for W-356 is smaller only by 3% from that for W-1000, while the experimental spontaneous polarization is decreased by 15% (at 317 K). It means that the decrease of  $P_s$  in W-356 lies not only in  $\langle \mu_\perp \rangle$  values of its components but also in differences in the molecular arrangement compared to W-1000, namely the lower tilt angle [Fig. 5(b)] and also lower values of the intralayer correlation length  $\xi$  [Fig. 9(d)].

The energy barriers calculated with the DFT-B3LYP/def2TZVPP method (Fig. 11) enable the interpretation of the dielectric relaxation processes in the overcooled and vitrified Sm-C<sub>A</sub>\* phase. The rotation of the benzene ring in the 3F5HPhF6 and 3F7FPhH6 molecules is connected with the energy barrier of 35 kJ/mol and 40 kJ/mol, respectively [Fig. 11(b)], which is close to the experimental activation energy of the  $\gamma$ -process (45–50 kJ/mol, obtained with uncertainty of 15%). The activation energy of the  $\beta$ -process, ca. 80 kJ/mol, is larger and implies the contribution of several intramolecular rotations to this process. The calculated energy barrier for rotation of biphenyl in the 3F5HPhF6 and 3F7FPhH6 molecules is equal to ca. 35 kJ/mol [if it is realized by simultaneous change of the  $\varphi_1$  and  $\varphi_3$  angles, Figs. 11(a) and 11(c)]. With assumption of the correlated rotation of the benzene ring and biphenyl, the energy barrier of 70 kJ/mol is obtained, approaching the activation energy of the  $\beta$ -process. Additionally, the energy barriers of 46 kJ/mol for rotation of benzene in C1 and of 43 kJ/mol for rotation of biphenyl in C2 are larger than respective values for 3F5HPhF6 and 3F7FPhH6, and this result agrees well with the increased activation energies of the  $\beta$ - and  $\gamma$ -processes in W-356. Since the  $\beta$ - and  $\gamma$ -process originate supposedly from rotations within the molecular core, it is assumed that the  $\alpha$ -process is related to collective movements of molecules around their long axes. At first, the  $\alpha$ - and  $\beta$ -processes can be modeled simultaneously based on the same intramolecular rotations, as it was shown for polymers in Ref. [85]. Second, the x-ray diffraction implies that the rotations around the short

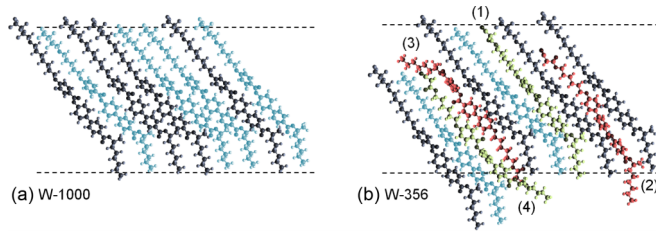


FIG. 12. Possible molecular packing of the components in one smectic layer of the  $\text{Sm-C}_A^*$  phase of the W-1000 (a) and W-356 (b) mixtures (in the neighbor layers, molecules are tilted in an opposite direction). Horizontal dashed lines indicate the smectic layer spacing. In the actual W-356 mixture, the concentration of the C1 and C2 components is lower. Although the presentations of structures are schematic, the proportions between the experimental layer spacing and the size of molecular models are preserved. The 3F5HPhF6, 3F7FPhH6, C1, and C2 molecules are marked as blue, black, green and red, respectively (a color figure available in the online version).

molecular axes are strongly hindered by the steric reasons, as the average distances between molecules within layers are 4.5–5 Å, which is only 10–15% of the molecular length. The rotations around the long axes are much more probable under such circumstances.

Finally, we would like to discuss the possible molecular arrangement in the W-1000 and W-356 mixtures. The experimental values of the smectic layer spacing  $d$  and tilt angle  $\Theta$  are related to the calculated molecular length  $L$  by the formula

$$\frac{d}{L} = \cos(\Theta - \delta\Theta), \quad (9)$$

where  $\delta\Theta$  allows us to include the nonlinear shape of molecules [47,74,86]. Taking into account both experimental and computational results for W-1000, it can be concluded that the 3F5HPhF6 and 3F7FPhH6 molecules form the smectic layers without dimer formation and without significant intercalation of the neighbor layers, as presented in Fig. 12(a). The results for W-356 imply that the arrangement of molecules in this mixture is more complex. The average length  $\langle L \rangle$  of the C1 and C2 molecules (distance between the two most distant atoms, excluding hydrogens), calculated as the Boltzmann average over extended conformations with different  $\varphi_3$  in 300 K, is equal to 37.6 Å and 37.4 Å, respectively. Meanwhile, the  $\langle L \rangle$  values for two main components are 37.7 Å and 40.3 Å for 3F5HPhF6 and 3F7FPhH6, respectively, and therefore the average molecular length over all components is smaller for the W-356 mixture than for W-1000. Because of that, one would expect smaller  $d$  values in W-356 than in W-1000, however, according to the XRD results, the layer spacing in W-356 is actually slightly larger [Fig. 9(c)]. Moreover, the additional low-angle peak in the XRD patterns of the  $\text{Sm-C}_A^*$  phase of W-356 implies the modulation of the smectic layers. The question is how the addition of the C1 and C2 compounds leads to these structural changes. The C1 molecule has a similar size to the 3F5HPhF6 molecule, therefore it can be easily implemented into the simple arrangement proposed for W-1000 [Fig. 12b(1)]. The C2 molecule is of the same size as C1, however, the position of the benzene ring and biphenyl with

respect to the chiral center is reversed in comparison with other components of W-356 (Fig. 1). Under the assumption that molecules prefer to be positioned so that the benzene ring from one molecule is in close proximity to the benzene ring from the neighboring molecule, to maximize the amount of the  $\pi$ - $\pi$  interactions, and similarly for the biphenyls, then the C2 molecules are likely to be either shifted along the molecular long axis [Fig. 12(2)] or rotated by 180° around the short axis with respect to other molecules [Fig. 12b(3)]. Additionally, the mesogens with  $-\text{C} \equiv \text{N}$  terminal groups are known of the tendency to dimer formation caused by dipole-dipole interactions [87,88], therefore the presence of C1-C1, C2-C2, or C1-C2 dimers within the W-356 mixture is likely [Fig. 12b(4)]. The implementation of the C1 and C2 molecules into the W-356 mixture, presented in Fig. 12b(2–4), disturbs the order within the smectic layer, which may cause the lower correlation length, tilt angle and spontaneous polarization as well as increase of the switching time [Figs. 5 and 9(d)] in W-356. Shifting of the C2 molecules [Fig. 12b(2)] can be related to the increased layer spacing, and the reversed position of the C2 molecule connected with the dimer formation with the C1 molecule [Fig. 12b(3,4)] is probably the explanation of the modulation of the smectic layers in W-356. The amount of the C1 and C2 components in W-356 is small, as for 1 mole of C2 there is 1.3 mole of C1, 8.0 mole of 3F7FPhH6 and 9.2 mole of 3F5HPhF6. This is why the main structural features, namely the smectic layer spacing, tilt angle and intralayer correlation length are only weakly modified in comparison to the base W-1000 mixture. At the same time, defects in the smectic layers in the W-356 mixture would explain the appearance of the low-angle diffraction peak well below the clearing temperature and its lowered intensity [Fig. 8(b)]. The inhomogeneity of the POM textures of the W-356 mixture [Fig. 3(b)] suggests that the number of defects shown in Fig. 12(b) varies in different parts of the sample.

#### IV. SUMMARY AND CONCLUSIONS

Two antiferroelectric liquid crystalline mixtures were investigated: W-1000, consisting of the 3F5HPhF6 and 3F7FPhH6 compounds in the 0.53 : 0.47 weight ratio, and W-356, consisting of the 3F5HPhF6, 3F7FPhH6, C1, and C2 compounds in the 0.47 : 0.43 : 0.06 : 0.04 weight ratio. The complementary methods such as differential scanning calorimetry, polarizing optical microscopy, electrooptic measurements, broadband dielectric spectroscopy, X-ray diffraction were used and the PM7 and DFT-B3LYP/def2TZVPP calculations were done. The main conclusions from the comparative study of the W-1000 and W-356 mixtures are as follows:

(i) W-1000 and W-356 exhibit during cooling the following phase sequence:  $\text{Iso} \rightarrow \text{Sm-A}^* \rightarrow \text{Sm-C}^* \rightarrow \text{Sm-C}_A^*$ , with lower transition temperatures for W-356. The glass transition of the  $\text{Sm-C}_A^*$  phase of both mixtures occurs at  $T_g \approx 230$  K, even for a very slow cooling. The cold crystallization after heating back above the glass softening temperature is not observed. Both samples remain in the  $\text{Sm-C}_A^*$  phase after keeping for 10 weeks in the room temperature, with prior cooling down to 150 K.

(ii) The W-356 mixture is characterized by the smaller tilt angle ( $\Theta_{\max} \approx 41^\circ$ ) and lower spontaneous polarization ( $P_{\max} = 182 \text{ nC/cm}^2$ ) than W-1000 ( $\Theta_{\max} \approx 43^\circ$ ,  $P_{\max} = 225 \text{ nC/cm}^2$ ). The switching time in both mixtures is equal to  $\tau_{\text{sw}} \approx 0.07 \text{ ms}$  in the vicinity of the clearing point and 1.5 and 1.8 ms for W-1000 and W-356, respectively, at 283 K.

(iii) The following dielectric relaxation processes were observed for the W-1000 and W-356 mixtures: the soft mode in the Sm-A\* and Sm-C\* phases; the Goldstone mode in the Sm-C\* phase; the X-process (low-frequency relaxation at the cell boundaries), the in-phase  $P_L$  phason, anti-phase  $P_H$  phason and the  $\alpha$ -process (collective movements around the long molecular axes) in the Sm-C<sub>A</sub>\* phase; the secondary  $\beta$ - and  $\gamma$ -process (rotations of benzene and/or biphenyl within the molecular cores) in the Sm-C<sub>A</sub>\* glass. The fragility index determined from  $\tau_\alpha(T)$  is  $m_f = 79$  and 73 for W-1000 and W-356, respectively, therefore W-356 is a slightly stronger glassformer, with lower tendency to potential cold crystallization.

(iv) X-ray diffraction results show that the glass transition of the Sm-C<sub>A</sub>\* phase leads to freezing of the intralayer movements of the whole molecules. However, the evolution of the low-angle peak from the smectic layer order does not stop below  $T_g$ , which implies that the arrangement of molecules in a direction perpendicular to the smectic layers is still changing in the vitrified Sm-C<sub>A</sub>\* phase.

(v) Diffraction patterns of W-356 imply the modulation of the smectic layers. It is caused probably by the reversed order of the benzene ring and biphenyl in the molecular core of the C2 component with respect to the C1, 3F5HPhF6 and 3F7FPhH6 molecules, and also by the dimer formation of the C1 and C2 compounds.

To sum up, this investigation confirms that the W-1000 mixture is a good candidate for application in displays, as

it is characterized by the stability of the high-tilted smectic-C<sub>A</sub>\* phase in the room temperature. The W-356 mixture has similar properties, however, it exhibits a lower tilt angle and slightly higher switching time. On the other hand, W-356 has a lower fragility index, which is an improvement compared to W-1000. It encourages to investigate other mixtures involving the 3FmX<sub>1</sub>PhX<sub>2</sub>6 compounds in search for even stronger glassformers, which at the same time preserve the orthoconic properties of W-1000.

Future investigations of the W-1000 and W-356 mixtures are going to be focused on the vibrational dynamics study carried out by the means of FT-IR spectroscopy together with the more complex DFT calculations for dimers. They are expected to give more insight into the evolution of the molecular arrangement during the glass transition and in the interactions leading to the hypothetical modulated lamellar structure in the W-356 mixture.

#### ACKNOWLEDGMENTS

We acknowledge Wojciech Zajac from the Institute of Nuclear Physics Polish Academy of Sciences in Kraków for help and discussion regarding the molecular modeling. The DFT calculations were performed at the Prometheus cluster from the Academic Computer Centre Cyfronet AGH (PL-Grid Infrastructure, grant plgmolkryst). Empyrean 2 (PANalytical) diffractometer with Cryostream 700 Plus (Oxford Cryosystems) attachment were purchased thanks to European Regional Development Fund Operational Program Infrastructure and Environment (Contract No. POIS.13.01.00-00-062/08). The authors declare no competing financial interest.

- 
- [1] N. A. Clark and S. T. Lagerwall, *Appl. Phys. Lett.* **36**, 899 (1980).
- [2] A. D. L. Chandani, Y. Ouchi, H. Takezoe, A. Fukuda, K. Terashima, K. Furukawa, and A. Kishi, *Jpn. J. Appl. Phys.* **28**, L1261 (1989).
- [3] A. D. L. Chandani, E. Górecka, Y. Ouchi, H. Takezoe, and A. Fukuda, *Jpn. J. Appl. Phys.* **28**, L1265 (1989).
- [4] K. D'have, P. Rudquist, S. T. Lagerwall, H. Pauwels, W. Drzewiński, and R. Dąbrowski, *Appl. Phys. Lett.* **76**, 3528 (2000).
- [5] S. Lagerwall, A. Dahlgren, P. Jägemalm, P. Rudquist, K. D'have, H. Pauwels, R. Dąbrowski, and W. Drzewiński, *Adv. Funct. Mater.* **11**, 87 (2001).
- [6] P. Rudquist, in *Handbook of Visual Display Technology*, edited by J. Chen, W. Cranton, and M. Fihn (Springer, Berlin, 2014).
- [7] H. Shi and S. H. Chen, *Liq. Cryst.* **19**, 849 (1995).
- [8] R. Elschner, R. Macdonald, H. J. Eichler, S. Hess, and A. M. Sonnet, *Phys. Rev. E* **60**, 1792 (1999).
- [9] H. M. P. Chen, D. Katsis, and S. H. Chen, *Chem. Mater.* **15**, 2534 (2003).
- [10] J. Wu, T. Usui, and J. Hanna, *J. Mater. Chem.* **21**, 8045 (2011).
- [11] R. Teerakapibal, C. Huang, A. Gujral, M. D. Ediger, and L. Yu, *Phys. Rev. Lett.* **120**, 055502 (2018).
- [12] Z. Chen, J. Yu, R. Teerakapibal, L. Meerpoel, and R. Richert, and L. Yu, *Soft Matter* **16**, 2025 (2020).
- [13] P. Perkowski, K. Ogrodnik, W. Piecek, Z. Raszewski, M. Żurowska, and R. Dąbrowski, *Mol. Cryst. Liq. Cryst.* **525**, 50 (2010).
- [14] W. Piecek, P. Perkowski, Z. Raszewski, P. Morawiak, M. Żurowska, R. Dąbrowski, and K. Czupryński, *Mol. Cryst. Liq. Cryst.* **525**, 140 (2010).
- [15] P. Perkowski, W. Piecek, Z. Raszewski, K. Ogrodnik, M. Żurowska, R. Dąbrowski, and J. Kędzierski, *Mol. Cryst. Liq. Cryst.* **541**, 191/[429] (2011).
- [16] W. Piecek, A. Bubnov, P. Perkowski, P. Morawiak, K. Ogrodnik, W. Rejmer, M. Żurowska, V. Hamplová, and M. Kašpar, *Phase Trans.* **83**, 551 (2010).
- [17] K. Ogrodnik, P. Perkowski, Z. Raszewski, W. Piecek, M. Żurowska, R. Dąbrowski, and L. Jaroszewicz, *Mol. Cryst. Liq. Cryst.* **547**, 54/[1744] (2011).
- [18] P. Perkowski, K. Ogrodnik, W. Piecek, M. Żurowska, Z. Raszewski, R. Dąbrowski, and L. Jaroszewicz, *Liq. Cryst.* **38**, 1159 (2011).

- [19] M. Czerwiński, M. Tykarska, R. Dąbrowski, A. Chelstowska, M. Żurowska, R. Kowerdziej, and L. R. Jaroszewicz, *Liq. Cryst.* **39**, 1498 (2012).
- [20] A. Chelstowska, N. Czerwiński, M. Tykarska, and N. Bennis, *Liq. Cryst.* **41**, 812 (2014).
- [21] P. Morawiak, M. Żurowska, and W. Piecsek, *Liq. Cryst.* **45**, 1451 (2018).
- [22] M. Żurowska, M. Czerwiński, J. Dziaduszek, and M. Filipowicz, *Phase Trans.* **91**, 521 (2018).
- [23] M. Urbańska, J. Dziaduszek, O. Strzeżysz, and M. Szala, *Phase Trans.* **92**, 657 (2019).
- [24] K. Kurp, M. Czerwiński, M. Tykarska, P. Salamon, and A. Bubnov, *J. Mol. Liq.* **290**, 111329 (2019).
- [25] M. Żurowska, R. Dąbrowski, J. Dziaduszek, K. Czupryński, K. Skrzypek, and M. Filipowicz, *Mol. Cryst. Liq. Cryst.* **495**, 145/497 (2008).
- [26] M. Żurowska, R. Dąbrowski, J. Dziaduszek, K. Garbat, M. Filipowicz, M. Tykarska, W. Rejmer, K. Czupryński, A. Spadło, N. Bennis, and J. M. Otón, *J. Mater. Chem.* **21**, 2144 (2011).
- [27] A. Deptuch, M. Marzec, T. Jaworska-Gołąb, M. Dziurka, J. Hooper, M. Srebro-Hooper, P. Fryń, J. Fitas, M. Urbańska, and M. Tykarska, *Liq. Cryst.* **46**, 2201 (2019).
- [28] M. Tykarska, M. Czerwiński, and A. Drzewicz, *J. Mol. Liq.* **292**, 110379 (2019).
- [29] K. Milewska, W. Drzewiński, M. Czerwiński, and R. Dąbrowski, *Liq. Cryst.* **42**, 1601 (2015).
- [30] J. Dziaduszek, R. Dąbrowski, K. Czupryński, and N. Bennis, *Ferroelectrics* **343**, 3 (2006).
- [31] W. Drzewiński, R. Dąbrowski, and K. Czupryński, *Polish J. Chem.* **76**, 273 (2002).
- [32] N. Osiecka, Z. Galewski, and M. Massalska-Arodź, *Thermochim. Acta* **655**, 106 (2017).
- [33] K. K. Raina and J. K. Ahuja, *Mol. Cryst. Liq. Cryst.* **338**, 125 (2000).
- [34] S. Khosla and K. K. Raina, *Indian J. Pure Appl. Phys.* **42**, 49 (2004).
- [35] T. Roisnel and J. Rodriguez-Carvajal, *Materials Science Forum* **378-381**, 118 (2000).
- [36] Gaussian 16, Revision C.01, M. J. Frisch, G. W. Trucks, H. B. Schlegel, G. E. Scuseria, M. A. Robb, J. R. Cheeseman, G. Scalmani, V. Barone, G. A. Petersson, H. Nakatsuji, X. Li, M. Caricato, A. V. Marenich, J. Bloino, B. G. Janesko, R. Gomperts, B. Mennucci, H. P. Hratchian, J. V. Ortiz, A. F. Izmaylov, J. L. Sonnenberg, D. Williams-Young, F. Ding, F. Lipparini, F. Egidi, J. Goings, B. Peng, A. Petrone, T. Henderson, D. Ranasinghe, V. G. Zakrzewski, J. Gao, N. Rega, G. Zheng, W. Liang, M. Hada, M. Ehara, K. Toyota, R. Fukuda, J. Hasegawa, M. Ishida, T. Nakajima, Y. Honda, O. Kitao, H. Nakai, T. Vreven, K. Throssell, J. A. Montgomery, Jr., J. E. Peralta, F. Ogliaro, M. J. Bearpark, J. J. Heyd, E. N. Brothers, K. N. Kudin, V. N. Staroverov, T. A. Keith, R. Kobayashi, J. Normand, K. Raghavachari, A. P. Rendell, J. C. Burant, S. S. Iyengar, J. Tomasi, M. Cossi, J. M. Millam, M. Klene, C. Adamo, R. Cammi, J. W. Ochterski, R. L. Martin, K. Morokuma, O. Farkas, J. B. Foresman, and D. J. Fox (Gaussian, Inc., Wallingford, CT, 2019), <https://gaussian.com/citation/>.
- [37] A. D. Becke, *J. Chem. Phys.* **98**, 5648 (1993).
- [38] C. Lee, W. Yang, and R. G. Parr, *Phys. Rev. B* **37**, 785 (1988).
- [39] F. Weigend and R. Ahlrichs, *Phys. Chem. Chem. Phys.* **7**, 3297 (2005).
- [40] S. Grimme, J. Antony, S. Ehrlich, and H. Krieg, *J. Chem. Phys.* **132**, 154104 (2010).
- [41] S. Grimme, S. Ehrlich, and L. Goerigk, *J. Comput. Chem.* **32**, 1456 (2011).
- [42] J. J. P. Stewart, *J. Mol. Model.* **19**, 1 (2013).
- [43] MOPAC2016, J. J. P. Stewart (Stewart Computational Chemistry, Colorado Springs, CO, 2016), <http://OpenMOPAC.net>
- [44] M. D. Hanwell, D. E. Curtis, D. C. Lonie, T. Vandermeersch, E. Zurek, and G. R. Hutchison, *J. Cheminform.* **4**, 17 (2012).
- [45] M. Jasiurkowska-Delaporte, E. Juszyńska, Ł. Kolek, J. Krawczyk, M. Massalska-Arodź, N. Osiecka, and T. Rozwadowski, *Liq. Cryst.* **40**, 1436 (2013).
- [46] K. D'havé, A. Dahlgren, P. Rudquist, J. P. F. Lagerwall, G. Andersson, M. Matuszczyk, S. T. Lagerwall, R. Dąbrowski, and W. Drzewiński, *Ferroelectrics* **244**, 115 (2000).
- [47] H. F. Gleeson, Y. Wang, S. Watson, D. Sahagun-Sanchez, J. W. Goodby, M. Hird, A. Petrenko, and M. A. Osipov, *J. Mater. Chem.* **14**, 1480 (2004).
- [48] J. K. Ahuja and K. K. Raina, *Jpn. J. Appl. Phys.* **39**, 4076 (2000).
- [49] V. M. Vaksman and Yu. P. Panarin, *Mol. Mats.* **1**, 147 (1992).
- [50] S. Havriliak and S. Negami, *J. Polym. Sci. C: Polymer Symposia* **14**, 99 (1966).
- [51] K. S. Cole and R. H. Cole, *J. Chem. Phys.* **9**, 341 (1941).
- [52] S. L. Srivastava and R. Dhar, *Indian J. Pure Appl. Phys.* **29**, 745 (1991).
- [53] C. Filipič, T. Carlsson, A. Levstik, B. Žekš, R. Blinc, F. Gouda, S. T. Lagerwall, and K. Sarp, *Phys. Rev. A* **38**, 5833 (1988).
- [54] S. M. Khened, S. Krishna Prasad, B. Shivkumar, and B. K. Sadashiva, *J. Phys. II* **1**, 171 (1991).
- [55] See Supplemental Material at <http://link.aps.org/supplemental/10.1103/PhysRevE.105.024705> for additional figures.
- [56] Yu. P. Panarin, O. Kalinovskaya, and J. K. Vij, *Liq. Cryst.* **25**, 241 (1998).
- [57] M. Buivydas, F. Gouda, G. Andersson, S. T. Lagerwall, B. Stebler, J. Bomelburg, G. Heppke, and B. Gestblom, *Liq. Cryst.* **23**, 723 (1997).
- [58] H. Uehara, Y. Hanakai, J. Hatano, S. Saito, and K. Murashiro, *Jpn. J. Appl. Phys.* **34**, 5424 (1995).
- [59] V. Novotna, M. Glogarova, A. M. Bubnov, and H. Sverenyak, *Liq. Cryst.* **23**, 511 (1997).
- [60] S. Kumari, I. M. L. Das, and R. Dąbrowski, *J. Mol. Liq.* **158**, 1 (2011).
- [61] Y. P. Panarin, H. Xu, S. T. M. Lughadha, and J. K. Vij, *Jpn. J. Appl. Phys.* **33**, 2648 (1994).
- [62] *Relaxation Phenomena. Liquid Crystals, Magnetic Systems, Polymers, High-Tc Superconductors, Metallic Glasses*, edited by W. Haase and S. Wróbel (Springer-Verlag, Berlin, 2003).
- [63] A. K. Jonscher, *J. Mater. Sci.* **16**, 2037 (1981).
- [64] M. Jasiurkowska-Delaporte, T. Rozwadowski, E. Dmochowska, E. Juszyńska-Gałązka, P. Kula, and M. Massalska-Arodź, *J. Phys. Chem. B* **122**, 10627 (2018).
- [65] T. Rozwadowski, M. Massalska-Arodź, Å. Kolek, K. Grzybowska, A. Bąk, and K. Chłędowska, *Cryst. Growth Des.* **15**, 2891 (2015).
- [66] M. Jasiurkowska-Delaporte, S. Napolitano, J. Leys, E. Juszyńska-Gałązka, M. Wübbenhorst, and M. Massalska-Arodź, *J. Phys. Chem. B* **120**, 12160 (2016).

- [67] A. Mishra, R. Dąbrowski, and R. Dhar, *J. Mol. Liq.* **249**, 106 (2018).
- [68] S. Lalik, A. Deptuch, P. Fryń, T. Jaworska-Gołąb, D. Dardas, D. Pocięcha, M. Urbańska, M. Tykarska, and M. Marzec, *Liq. Cryst.* **46**, 2256 (2019).
- [69] D. Georgopoulos, S. Kriptomou, E. Argyraki, A. Kyritsis, and P. Pissis, *Mol. Cryst. Liq. Cryst.* **611**, 197 (2015).
- [70] A. Drzewicz, M. Jasiurkowska-Delaporte, E. Juszyńska-Gałązka, W. Zając, and P. Kula, *Phys. Chem. Chem. Phys.* **23**, 8673 (2021).
- [71] J. J. Moura Ramos and H. P. Diogo, *Mol. Cryst. Liq. Cryst.* **571**, 19 (2013).
- [72] R. Böhmer, K. L. Ngai, C. A. Angell, and D. J. Plazek, *J. Chem. Phys.* **99**, 4201 (1993).
- [73] H. Tanaka, *J. Non-Cryst. Solids* **351**, 678 (2005).
- [74] A. Deptuch, T. Jaworska-Gołąb, M. Marzec, D. Pocięcha, J. Fitas, M. Żurowska, M. Tykarska, and J. Hooper, *Phase Trans.* **91**, 186 (2018).
- [75] A. Deptuch, M. Jasiurkowska-Delaporte, W. Zając, E. Juszyńska-Gałązka, A. Drzewicz, and M. Urbańska, *Phys. Chem. Chem. Phys.* **23**, 19795 (2021).
- [76] A. Deptuch, M. Jasiurkowska-Delaporte, E. Juszyńska-Gałązka, A. Drzewicz, W. Zając, and M. Urbańska, *Crystals* **11**, 1487 (2021).
- [77] G. P. Johari and M. Goldstein, *J. Chem. Phys.* **53**, 2372 (1970).
- [78] K. L. Ngai and M. Paluch, *J. Chem. Phys.* **120**, 857 (2004).
- [79] K. L. Ngai and S. Capaccioli, *Phys. Rev. E* **69**, 031501 (2004).
- [80] G. Williams and D. C. Watts, *Trans. Faraday Soc.* **66**, 80 (1970).
- [81] F. Alvarez, A. Alegria, and J. Colmenero, *Phys. Rev. B* **44**, 7306 (1991).
- [82] L. M. Blinov, *Structure and Properties of Liquid Crystals* (Springer Science+Business, Media B.V., 2011).
- [83] S. Lalik, A. Deptuch, T. Jaworska-Gołąb, P. Fryń, D. Dardas, O. Stefańczyk, M. Urbańska, and M. Marzec, *J. Phys. Chem. B* **124**, 6055 (2020).
- [84] Y. Takanishi, A. Ikeda, H. Takezoe, and A. Fukuda, *Phys. Rev. E* **51**, 400 (1995).
- [85] G. D. Smith and D. Bedrov, *J. Polym. Sci. Part B: Polym. Phys.* **45**, 627 (2007).
- [86] D. Ziobro, R. Dąbrowski, M. Tykarska, W. Drzewiński, M. Filipowicz, W. Rejmer, K. Kuśmierk, P. Morawiak, and W. Piecek, *Liq. Cryst.* **39**, 1011 (2012).
- [87] P. Patel, L. Chen, and S. Kumar, *Phys. Rev. E* **47**, 2643 (1993).
- [88] Y. Lansac, M. A. Glaser, and N. A. Clark, *Phys. Rev. E* **64**, 051703 (2001).